Received: 26 August 2022 | Revised: 24 October 2022 | Accepted: 25 October 2022

DOI: 10.1002/eng2.12590

RESEARCH ARTICLE

Engineering Reports Open Access WILEY

Experimental application of a laser-based manufacturing process to develop a free customizable, scalable thermoelectric generator demonstrated on a hot shaft

Marvin Abt[1] | **Katharina Kruppa**[2] | **Mario Wolf**[2] | **Armin Feldhoff**[2] | **Ludger Overmeyer**[3]

[1]Institut für Integrierte Produktion Hannover gGmbH, Hannover, Germany

[2]Institute of Physical Chemistry and Electrochemistry, Leibniz University Hannover, Hannover, Germany

[3]Institute of Transport and Automation Technology, Leibniz University Hannover, Hannover, Germany

Correspondence
Marvin Abt, Institut für Integrierte Produktion Hannover gGmbH, Hannover, Hollerithallee 6, Germany.
Email: abt@iph-hannover.de

Funding information
Deutsche Forschungsgemeinschaft, Grant/Award Number: 325156807

Abstract

Geometry, design, and processing in addition to the thermoelectric material properties have a significant influence on the economic efficiency and performance of thermoelectric generators (TEGs). While conventional BULK TEGs are elaborate to manufacture and allow only limited variations in geometry, printed TEGs are often restricted in their application and processing temperature due to the use of organic materials. In this work, a proof-of-concept for fabricating modular, customizable, and temperature-stable TEGs is demonstrated by applying an alternative laser process. For this purpose, low temperature cofired ceramics substrates were coated over a large area, freely structured and cut without masks by a laser and sintered to a solid structure in a single optimized thermal post-processing. A scalable design with complex geometry and large cooling surface for application on a hot shaft was realized to prove feasibility. Investigations on sintering characteristics up to a peak temperature of 1173 K, thermoelectric material properties and temperature distribution were carried out for a $Ca_3Co_4O_9$/Ag-based prototype and evaluated using profilometer, XRD, and IR measurements. For a combined post-processing, an optimal sintering profile could be determined at 1073 K peak temperature with a 20 min holding time. Temperature gradients of up to 100 K could be achieved along a thermocouple. A single TEG module consisting of 12 thermocouples achieved a maximum power of 0.224 μW and open-circuit voltage of 134.41 mV at an average hot-side temperature of 413.6 K and temperature difference of 106.7 K. Three of these modules combined into a common TEG with a total of 36 thermocouples reached a maximum power of 0.58 K and open-circuit voltage of 319.28 mV with a lesser average hot-side temperature of 387.8 K and temperature difference of 83.4 K.

KEYWORDS

$Ca_3Co_4O_9$, energy harvesting, laser structuring, LTCC, printed ceramics, thermoelectric generator

1 | INTRODUCTION

1.1 | Application of thermoelectric generators

The supply of energy from nonfossil sources, its effective use and recovery are essential in the transformation to a low-emission economy while energy consumption is constantly rising at the same time.[1] According to the International Energy Agency, photovoltaics or wind energy are providing an increasing share of primary energy worldwide,[2] while thermoelectrics successfully fill niches in the field of energy harvesting. Energy harvesting is the conversion of small amounts of abundant into electrical useful energy. In the case of thermoelectrics, thermal energy from the environment is used, which is exchanged between objects of different temperatures.

Compared to other supply technologies, thermoelectric generators (TEGs) generally can only provide small amounts of electrical power.[3] Depending on the material and ambient conditions the technically realizable efficiency in practice is below 5%.[4,5] By using finite element method (FEM) optimized geometry and improved material values over 10% have already been reached under operational conditions.[6,7] Despite these advances, TEGs are not often used to independently supply larger electrical loads except for some special applications like the powering of space exploration missions using radioisotope heat sources.[8,9] One focus of their application is the partial recovery of waste heat where it already occurs in large flows, such as in energy-intensive industrial processes or combustion engines.[10,11] According to estimates over 50% of global primary energy production could be lost in the form of waste heat.[12] The second main application of TEGs is to provide minimal amounts of energy for autonomous powering of small electrical loads. An increasing number of studies have investigated the application of TEGs, for example to supply energy-autonomous wireless sensor networks (WSN)[13,14] or body sensors.[15,16] At present, sensor nodes are still usually limited by their battery capacity and maintenance requirements, hence a lot of effort is spent on minimizing their energy consumption.[17,18]

TEGs have no moving parts, require no maintenance and can replace batteries in many applications and environments that are difficult to access.[19,20] However, they are not suitable for every environment. TEGs require a permanent heat source and heat sink which are accessible by the generator.

1.2 | Processing of TEGs

The structure and geometry of conventional TEGs limit the choice of suitable application environments. The processing of thermoelectric materials such as bismuth telluride include their bonding and assembly to the TEG are complex and cost-intensive.[21] Generators fabricated in this way have sufficiently high efficiencies for most applications—but they are restricted in geometry, rigid, and planar.[22,23] Although they cover a wide range of applications conventional TEGs are not suitable for many environments or surfaces due to these limitations.

This is one of the reasons why alternative manufacturing processes and TEG designs are the focus of research. Depending on the approach they ensure better processability, simple scalability, alternative geometries, and other materials. Printing processes in particular are discussed in this context. They allow depositing thermoelectric structures additively on a substrate. Several different technologies such as dispense printing,[24,25] ink-jetting,[26,27] aerosol printing,[28] or screen printing[29,30] have been investigated for the manufacturing of film-based TEG. By using printing technologies new TEG designs could be established especially in combination with flexible polymer substrates. These include radial generators,[31,32] roll-to-roll generators,[33] or foldable designs.[30,34] Although in many cases these approaches allow more flexibility in geometry and material selection and provide a more targeted design,[35] they have not yet established themselves on the market. A major reason for this is the high difference in reachable electrical power outputs between conventional and printed TEGs.[29,36,37] On the material level, this is characterized by the power factor *PF* of the thermoelectric materials:

$$PF = \sigma^* \alpha.^2 \tag{1}$$

The power factor is defined by the electrical conductivity σ and the Seebeck coefficient α. The material properties of printed thermoelectric films are, as a result of the process, below those of bulk materials as used in conventional TEGs.[29]

In special, the electrical conductivity is degraded by the porosity of the films and the additives and binders required in the inks.[29,38]

Although many studies have demonstrated that printed TEGs can in principle be suitable for a variety of low-power applications, the development of printing inks can be a big challenge. Depending on the specific process, the inks must be customized to many parameters such as particle size distribution, viscosity, thixotropy, surface tension, oxidation stability, and dispersion stability.[35,39] The additives and binders required for this not only reduce the thermoelectric properties. But the formulation of ink systems is also a time-consuming and challenging process which affects the availability and the costs of the inks.

Furthermore, the choice of substrate has a great influence on the processing and properties of thermoelectric films. If flexible polymer substrates are used, thermal post-processing for debinding and sintering of the films is very limited because of the low thermal stability.[15,23] An interesting and underestimated alternative for this can be low temperature cofired ceramics (LTCC) substrates. These substrates are flexible films of ceramic particles embedded in a polymer matrix. During thermal post-processing, ceramic particles are debinded and then sintered into a temperature resistant and solid structure. The laser material processing of LTCC substrates is an established technology in special PCB manufacturing and has already been investigated.[40] Independent of TEG manufacturing some work has also addressed laser structuring of electronic thick films on LTCC substrates in general[41] or for applications, such as to generate microwave circuits[42] or microstructured low-pass filter.[43] An adaptation of LTCC technology and laser processing to TEG manufacturing has significant potential for several reasons. First, it is possible to cut the substrate to any shape and to generate the thermoelectric structures freely and maskless at high processing speed. Second, the substrate is flexible at the beginning and can tolerate a thermal post-processing with temperatures above 1000 K in comparison to polymer substrates. Third, as demonstrated by Gutzeit et al., very small structures of up to 25 µm widths can be theoretically realized by laser structuring with suitable equipment,[41] which is comparable to or smaller than the resolution of practically available screen-printing processes (~ 100 µm[44]).

Some studies have already successfully demonstrated the capability of LTCC substrates for the manufacturing of TEG by using existing printing technologies. Jaziri et al. presented one Ag/PdAg and one Ag/Ni-based TEG with 104 thermocouples on a LTCC substrate, which was fabricated by screen printing.[45] The first one achieved an electrical power output of 81 µW at a temperature gradient of 114 K, while the AgNi-based one achieved an electrical power of 4.6 µW at 62 K difference. Markowski also demonstrated a screen-printed Ag/PdAg-based TEG. This was made of up to three LTCC layers with 30 thermocouples each.[46] A laminate of three layers and 90 thermocouples achieved an electrical power of 0.46 mW at a temperature difference of 193 K.

1.3 | Laser-structured TEG

In previous work, the authors presented an alternative process to established printing technologies for the manufacturing of film-based TEG.[47,48] It combines large scale spray-coating with selective laser structuring on LTCC substrate and is illustrated in Figure 1.

As a subtractive process the method presented here is different from additive printing methods, particularly in the application of thermoelectric materials. The material application by spray-coating (Figure 1A) and the generating of thermoelectric structures by laser structuring (Figure 1B) are executed independently of each other. Printing processes usually have to use significant amounts of organic additives and binders to adjust viscosity and thixotropy in order to prevent the structures from bleeding.[49] This is not necessary for large-scale spray coating, so the inks used can have lower viscosities, material loadings, and amounts of additives and binders. The spray-coating process is continuous at high feed rates, which has benefits for film homogeneity and process stability.[50] The lower requirements of spray-coating also simplify the formulation of new inks with other material systems.

The thermoelectric material system used includes calcium cobalt oxides (CCO) on the front side and silver on the back side. Although CCO achieves only moderate performance in the addressed temperature range below 500 K,[51] the combination is well suited for demonstrating the technology and enables comparison to the traditional TEG design. Both CCO and silver are nontoxic and can therefore be applied with basic equipment via spray-coating. For example, the Ni-based systems presented by Jaziri et al. have high requirements for the equipment due to their toxicity in a spray process. In addition, thermal post-processing of CCO, Ag, and LTCC substrate can be realized in the single common processing step due to overlapping sintering ranges.[41]

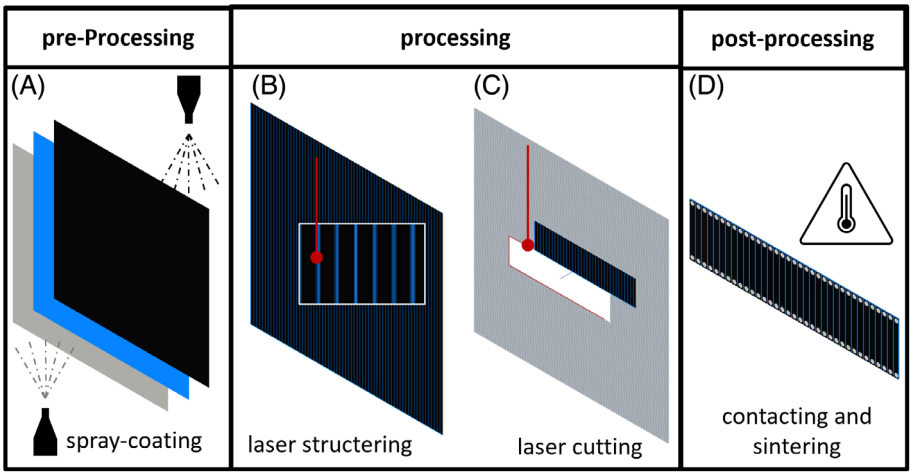

FIGURE 1 Combined spray-coating and laser structuring by Abt and Wolf[47,48] (A): Large-scale spray-coating of an unsintered LTTC substrate (blue) on both sides with different thermoelectric materials (gray, black). (B): Selective ablation of the films by laser structuring to create the thermoelectric structures. (C): Free cutting of the substrate by a laser process. (D): Thermal sintering of substrate and structured films. Contacting of thermoelectric structures on front and back side by using vertical interconnects (VIAS) or edge dipping.

The geometry of the previously presented TEG was based on traditional TEG designs and did not utilize the flexibility of the process.[48] With suitable parameterization, the combination of LTCC technology and laser processing enables the fabrication of almost any 2D geometry without the use of masks. Neither in our own preliminary work nor in other studies was this potential utilized. A generator manufactured in this way can be designed with minimal effort and without being thermally limited in its application by a flexible polymer substrate. This high level of flexibility allows TEGs to be individually designed for their specific application environment. This is in direct contrast to conventional BULK-TEGs, which place high requirements on their contact areas due to their rigid and planar shape.

Here we present a proof-of-concept which shows how laser material processing and LTCC technology can be used to design thermoelectric generators which are modular, scalable and customizable to the application environment and surface. The presented TEG uses a modular design. Multiple TEG modules can be combined in an electrical series connection to increase the power output. At the same time the modularization of the TEG allows to minimize the manufacturing risk since in case of a partial defect only one module has to be discarded and not the whole generator. The structure of a single module is shown in Figure 2.

The chosen application scenario contains thermoelectric energy harvesting on a hot pipe or shaft, as it is often the case in production plants or combustion processes. A heat flow is absorbed by the inner tube via brass rings and flows outwards via the module, where it is emitted into the ambient air. This creates a temperature gradient along the straight CCO structures on the front side and generates a thermoelectric potential. Via vertical interconnects (VIAS) and silver structures on the backside, the electric current is returned to the center of the module. Cross bracing stabilizes the module and enables the series connection of the thermocouples.

The geometry of the modules is inspired by the design of heatsinks. Conventional TEGs use massive metallic cooling structures to dissipate heat to the environment and create a temperature gradient.[52] LeBlanc et al. analyzed that up to two-thirds of the total system cost of a conventional TEG is spent on isolating ceramic plates and heatsink.[53] In contrast, the modules presented here do not require any of these components and integrate the function of a heatsink through their design and a maximized surface. This demonstrates how the flexibility of the manufacturing process can be used for innovative and individualized TEG geometries.

A module includes 12 thermocouples (Figure 2). Each thermocouple generates a voltage along its length, which is dependent on the Seebeck coefficients α of the materials on the front and back side and increases with the temperature difference. Multiple modules can be combined to build a stacked TEG as needed. Figure 3 shows the assembly of 3 single modules with 36 thermocouples, which are combined into one stacked TEG (3-Stack).

In the current set-up, the electrical contact between two modules is established via the rings between them. To reduce the resistances, the contact surfaces of the rings and modules were coated with a conductive silver layer before

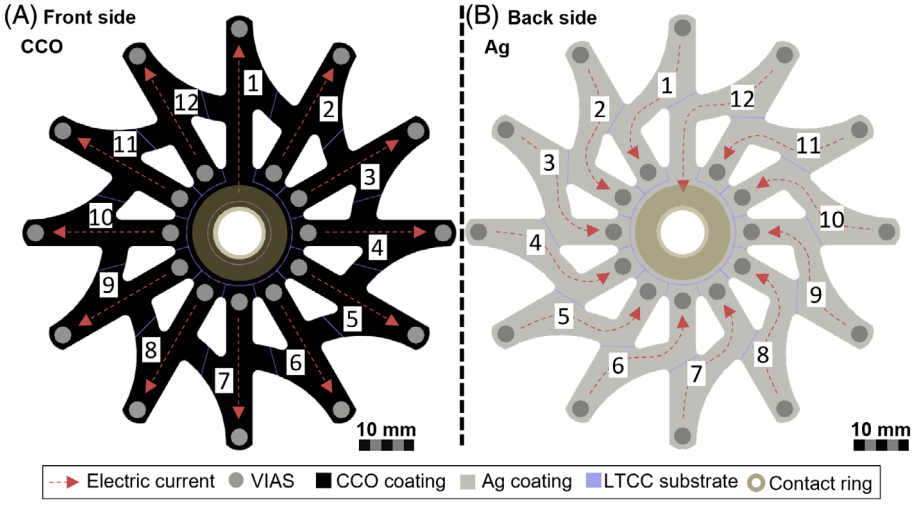

FIGURE 2 Symmetrical TEG module with 12 thermocouples: The electric flow along the numbered couples is shown by red arrows. The electrical contact is realized via a brass ring in the center of the front side (A) of the module to the first thermocouple. VIAS inside and outside contact through the LTCC substrate to the backside of the TEG module (B). On the back side, a contact is set up to a brass ring at the 12th thermocouple in the center of the module.

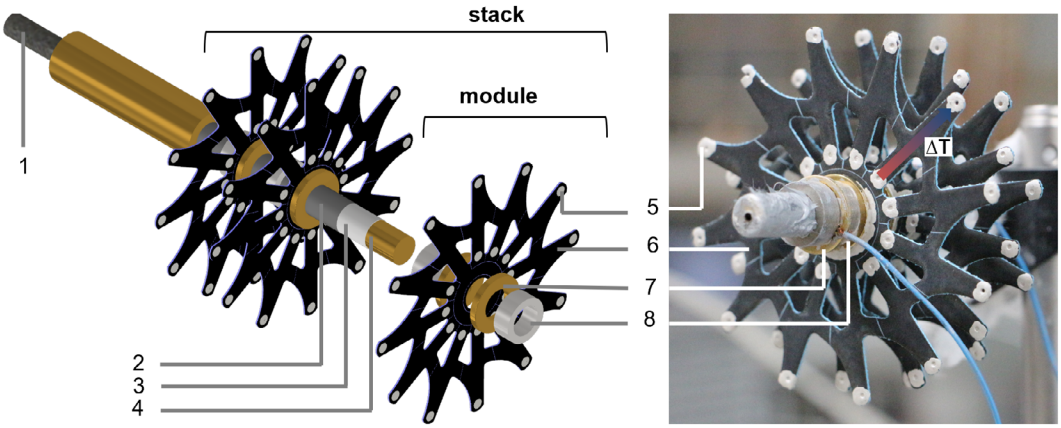

FIGURE 3 Stacked TEG with 3 modules (3-Stack): The shaft (4) is heated by a heating element (1). This is coated with a temperature-resistant thin ceramic coating (3) (Cemera DIP 528-N, ca. 150 µm). Brass rings (7) at the front side and back side connect the modules (6) electrically and transfer the heat via their inner surfaces. SmCo17- ring magnets (8) work as spacers, keep the modules in position and transfer heat to the brass rings. A thermal gap filler (3) minimizes the thermal resistance between the shaft and the inside of the rings. Within a module, the front side and back side thermocouples are contacted by vertical interconnects (VIAS) (5) (cf. Figure 2).

assembly. The magnets create a high contact pressure and hold all components securely in place. As shown in Figure 4, the electrical current flows along the modules and the rings and the voltage is measured at the front and rear ring of the stack.

2 | EXPERIMENTAL SECTION

2.1 | Materials and components

Unless otherwise mentioned, all reagents obtained from commercial vendors were reagent grade or higher and used without further purification. CCO from CerPoTech (Tiller, Norway) was used. For the spray-coating the powder was dispersed with 30 w% into isopropanol under stirring and with ultrasonic treatment before application. The silver coating

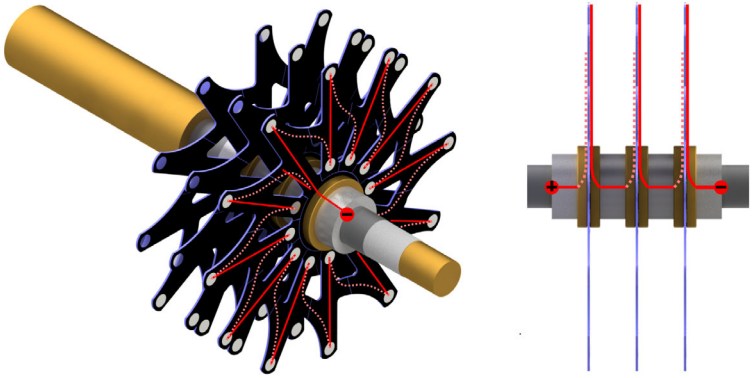

FIGURE 4 Electric current flow inside a TEG stack of three modules. On the front side of each thermocouple, a potential is generated by p-type CCO, over which the current flows in a closed circuit (red lines). On the back, silver is used to conduct to the next thermocouple (bright dotted line). Two modules are connected to each other via the back side of the 12th thermocouple and the front side of the first thermocouple. In between, the metallic rings provide the electrical contact.

was applied using silver spray from MARAWE, bonding via VIAS with 2200 MTP silver ink from CircuitWorks. The LTCC substrate was a 2-layer laminate of Dupont 951 PX. The shaft had a diameter of 8 mm and was made of copper or brass. For electrical isolation, this was coated with a high-temperature stable ceramic coating (Cemera DIP 538-N from aremco with 10 w% dist. H_2O). The coating thickness was below 150 µm. A silicone-free thermal gap filler, which is specified up to 623 K, was applied between the TEG and the shaft. The rings on the front and back sides of the modules are made of brass according to DIN 125 M8. Temperature stable SmCo17 ring magnets with an inner diameter of 8.5 mm were placed between the modules. The shaft was heated by a 40 W element with a diameter of 6.5 mm and a length of 45 mm. The power was controlled by a Hotset C 448/2. A type K thermocouple was mounted in a hole on the face in the shaft and measured the core temperature.

2.2 | Processing

The substrate was tempered to 373 K and spray-coated in a previously presented method.[47] The coated LTCC substrates can be processed immediately. Structuring and cutting were performed with a ZING 16 CO_2 laser from Epilog with 40 W nominal power and active air assist. The spot diameter was 120 µm. The parameters are based on the findings from preliminary work[47,48] and other studies on laser processing of LTCC.[40–43,54–56] In particular, when CO_2 lasers are used, a high amount of thermal energy is dissipated into the surrounding areas of the LTCC substrate due to the large wavelength and long pulse durations.[40] When cutting the LTCC substrate, the binder matrix is thermally removed and ceramic particles are deposited.[42,55] To minimize the heat input into the surrounding substrate, high speeds (max. 200 mm/s) and frequencies (max. 5000 Hz) are preferred.[42] A second cycle can be used to couple in additional energy to ensure that the substrate is reliably cut off. Exposed ceramic particles are removed by the air assist. However, when structuring, only a few micrometers of the CCO and silver films are ablated. For this reason, the speed is at a maximum and the laser power is significantly lower. In order to avoid damaging the substrate below, only the minimum necessary laser power is used.[40,54] Metallic particles have significantly lower absorption rates with CO_2 lasers,[57] therefore the laser power must be chosen higher than CCO. The process parameters used for laser structuring and laser cutting are listed in Table 1.

TABLE 1 Process parameters for film structuring and laser cutting of the substrate

Material	Mode	Average speed [mm*s^{-1}]	Average power [W]	Frequency [Hz]	Cycles
LTCC: DuPont 951 PX, 2-layer	Cutting	150	36	5000	2
Calcium cobalt oxide: CerPoTech CCO (Tiller, Norway)	Structuring	200	1.8	500	1
Silver: Marawe silver spray	Structuring	200	3.6	500	1

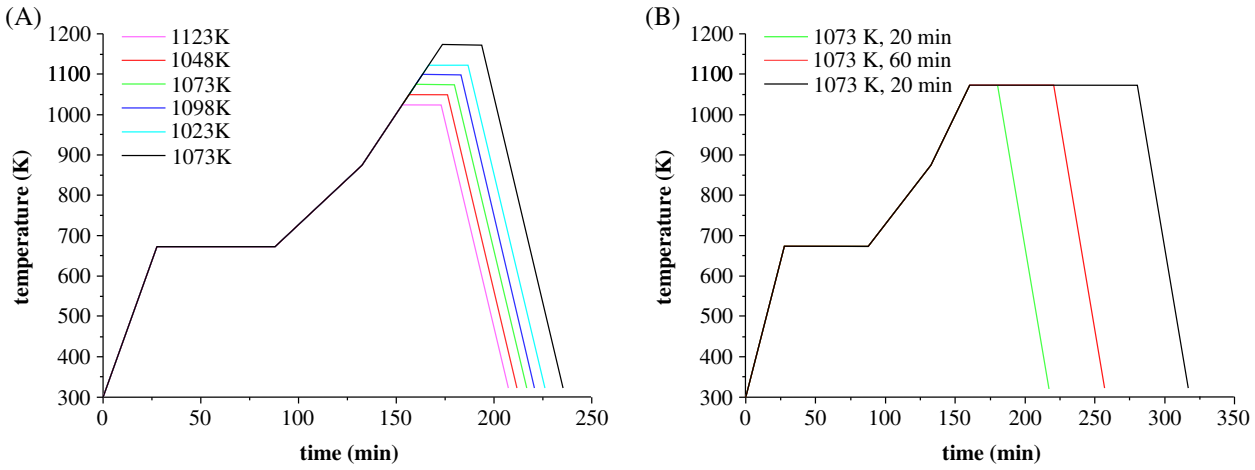

FIGURE 5 (A) Sintering profiles with different maximum temperature T_{max}. (B) Sintering profiles with different duration at constant maximum temperature $T_{max} = 1073$ K. The profiles are based on the design rules of the LTCC substrate.[58]

Thermal post-processing of LTCC substrate, CCO, and silver films were performed in a single process. The cut and structured TEG modules were each placed between two Al_2O_3 plates with dimensions 100 mm × 100 mm × 6 mm (Schuba AP-92).The sintering profiles follow the manufacturer's design rules, but maximum temperature and duration at maximum temperature were varied.[58] The sintering profiles considered in the following are shown in Figure 5.

2.3 | Characterization

The geometry of the TEG modules was measured before and after thermal post-processing using a VR-5000 profilometer from KEYENCE and a micrometer gage (Mitutoyo 0–25 mm 1,204,565). By using a thermocouple type K the ambient temperature was documented during the experimental procedure. Thermographic measurements on the TEG were made with a VarioCAM HD from InfraTEC at a resolution of 640 × 480 pixels. CCO films were applied to alumina slides by spray coating to investigate the influence of sintering temperature and holding time (cf. Figure 5). These films were characterized by x-ray diffraction (XRD, Bruker D8 Advance with Cu-Kα radiation). The Seebeck coefficient α and the power factor PF of the CCO were measured as a function of temperature using a ProboStat A setup of NorECs with ELITE thermal system and KEITHLEY 2100 digit multimeters. The isothermal electrical conductivity σ of CCO was investigated with a home-built modified van-der-Paul measuring cell with a horizontal carbolite tube furnace and KEITHLEY 2100 digit multimeters. Current and voltage of the assembled TEG were measured for different load resistors via a resistor cascade (R1-1000 Mini from cmt) and already above-mentioned multimeters. All thermography and power measurements were carried out in steady state conditions after 45 min and under free convection. For the *U-Iq* and power output curves Figure 10 linear fits and second-degree polynomial fits were used, respectively.

3 | RESULTS AND DISCUSSION

Figure 3 illustrates that each TEG module has two contact surfaces to the brass rings and one to the shaft. Their dimensions and tolerances must be known so that the modules can be combined into a single TEG stack. However, LTCC substrates have a characteristic shrinkage during debinding and sintering, which strongly depends on the parameters of the sintering profile used. Because LTCC substrate, CCO film and silver film are processed in a single thermal post-processing there are several conditions that must be fulfilled:

- Binders and additives from the LTCC substrate and silver film must be removed completely.

- LTCC substrate, CCO, and silver film must be sintered into solid structures.
- Both films must stay thermally stable.
- The electrical conductivity σ and the power factor PF of the CCO film should be optimized in accordance with the previous conditions.

The evaporation and decomposition of the organic components from the LTCC substrate and silver film occurs up to a temperature of approx. 650 K. This is significantly below the temperatures known for sintering of the LTCC substrate and the CCO. For the LTCC substrate, the manufacturer provides a maximum temperature of approx. 1123 K for a duration of 20 min (Figure 5A).[58] Tahashi et al. investigated the temperature dependence of CCO sintering and determined the range from 1073 to 1193 K as the optimum for the maximum temperature with the greatest possible power factor.[59] They also showed that a decomposition reaction to $Ca_3Co_2O_6$ begins at above 1193 K. Although an oxidation reaction does not occur in silver above 423 K,[60] silver films can lose stability in dependence on the layer thickness above approx. 873 K with increasing temperature and duration of the sintering process due to agglomeration processes.[61] A combined sintering profile must therefore choose a sufficiently high maximum temperature and duration for the CCO so that the thermoelectric material properties are sufficiently developed, while at the same time keeping the range above approx. 873 K as short as possible to minimize the risk of damage to the silver film.

Figure 5 shows sintering profiles varying in maximum temperature (5A) and duration (5B), which were investigated for CCO. CCO films were applied to Al_2O_3 slides and processed according to the sintering profiles. The films were analyzed by XRD and are shown in Figure 6.

The measurements show that diffraction peaks corresponding to CCO can be detected an increase in the intensity of the characteristic 0020 and 0040 reflections with increasing sintering temperature starting at 1073 K (Figure 6A) and also with rising sintering duration (Figure 6B). Over all measurements, no signals could be identified that indicate contamination or decomposition of the CCO. The results are confirmed by the previously mentioned literature values. However, the thermoelectric properties of the CCO cannot be inferred directly from the dimension of the CCO platelets.

Figure 7 presents the resulting electrical conductivity σ, Seebeck coefficient α and power factor PF as a function of temperature for the different maximum sintering temperatures and durations. Both the electrical conductivity (Figure 7A) and the resulting power factor (Figure 7B) collapse below 1023 K. This can be explained by the missing sintering and corresponding increase of CCO platelet size observed in the XRD measurements. In particular, the

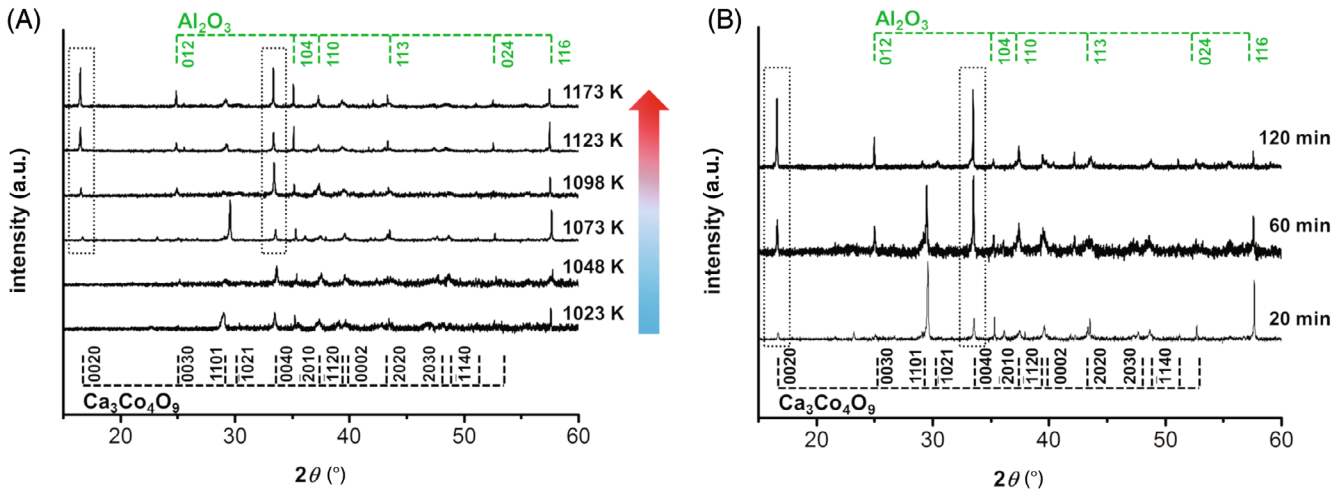

FIGURE 6 XRD measurement of the sintering characteristics of CCO. (A) For varying maximum sintering temperatures and (B) for varying sintering durations. Compare also sintering profiles shown in Figure 5. Dashed lines show the literature reflections and indices of $Ca_3Co_4O_9$ (PDF: 00-062-0692) and Al_2O_3 (PDF: 01-075-1865). Reflections of CCO correspond to the superspace group Cm (0 1 -p 0).[62] The characteristic 0020 and 0040 reflections that showcase the sintering of the CCO plates with strongly increasing intensity are marked.

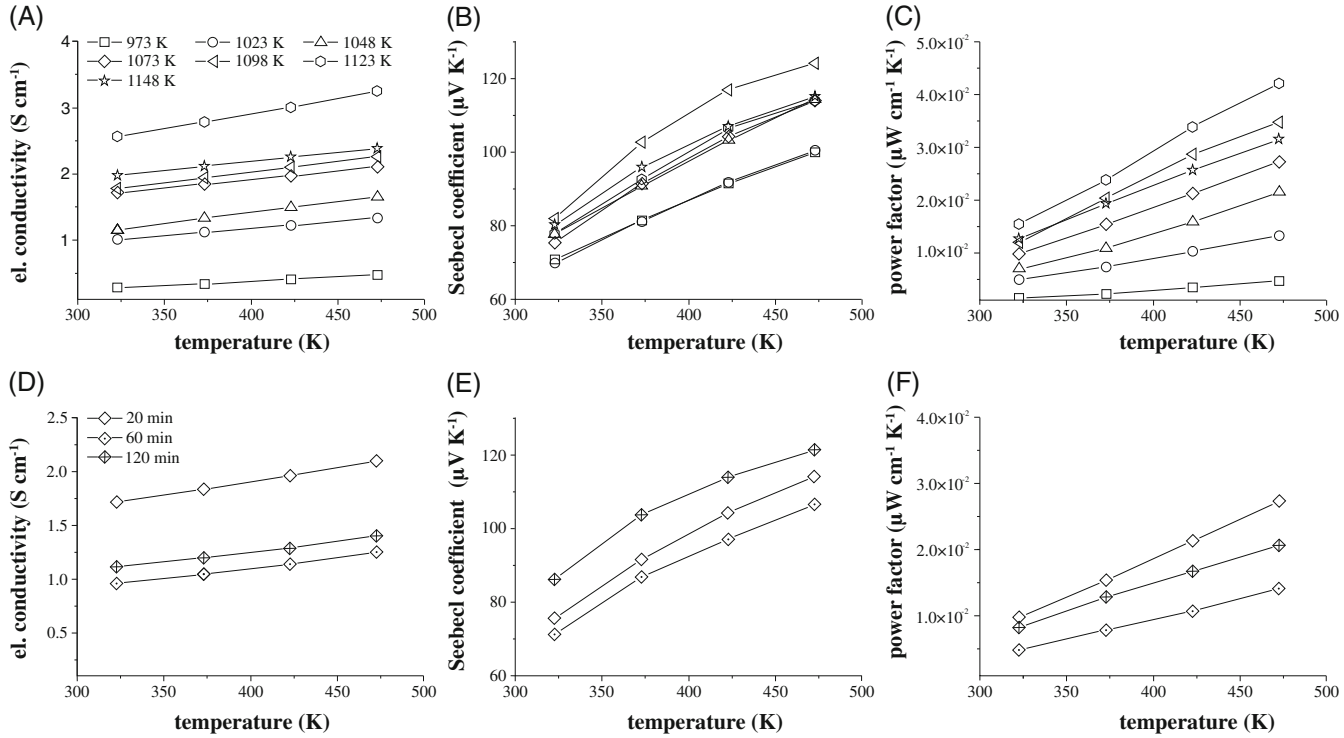

FIGURE 7 Thermoelectric material properties for different maximum temperatures and durations during post-processing. (A–C) Electrical conductivity σ (A), Seebeck coefficient α (B), and power factor *PF* (C) for different maximum temperatures. The sinter profiles correspond to the graphs in Figure 5A. (D–F) Electrical conductivity σ (D), Seebeck coefficient α (E), and power factor *PF* (F) for different duration at a maximum temperature of 1073 K. The sintering profiles correspond to the graphs in Figure 5B.

power factor *PF* increases strongly up to a maximum temperature of 1073 K and then grows moderately. On the other hand, a comparison of different durations at a maximum temperature of 1073 K shows that a longer duration at maximum temperature does not have a positive effect on the electrical conductivity σ (Figure 7D) and the power factor *PF* (Figure 7F). As the XRD measurement shows increased platelet growth, this may indicate increased cracking of the film. However, a profiliometer measurement could not confirm the existence of cracks in a µm scale. It is also possible that the sintering of the CCO platelets is overlaid with a temperature- and time-dependent degenerative effect, which is caused by organic residues of the substrate or a changed atmosphere composition. This should be investigated in a future study.

Furthermore, a reduction of the layer thickness from 15 µm (20 min) to 12 µm (60 min), to 10 µm (120 min) could be measured for the samples from Figure 7C–F, while at different maximum temperatures (Figure 7A–C) the layer thicknesses of the samples were constant at 15 µm. Based on the measurements the sintering profile with a maximum temperature of 1073 K for 20 min was chosen for a combined thermal post-processing of LTCC substrate, CCO film, and silver film.

Using the selected sinter profile, the relevant parameters for the design of the laser process were defined. Ten samples of 25 mm × 20 mm were coated with a CCO film and structured with a stripe pattern by a laser. Post-processing was carried out with the chosen sintering profile. The samples were measured before and after sintering using a profilometer. From the comparison of the given pattern, the unsintered and the sintered samples, the cutting loss, the structuring width, and the characteristic shrinkage were calculated (Table 2).

The shrinkage of the substrate with a factor of 0.89 is slightly lower than specified by the manufacturer's value of 0.87.[58] This can be explained by the fact that the maximum temperature of the selected sintering profile remains below the manufacturer's specification. Considering the cutting losses and the tolerances, a cutting pattern for the TEG modules was generated based on the scaling factor. The modules manufactured in this way and the TEGs which are assembled from them are shown in Figure 8.

A measurement of the dimensions of the module presented in Figure 8A shows that the shrinkage due to the thermal post-processing of the module is reproducible for the sintering profile within the specified tolerances. Compared to the

TABLE 2 Parameters for laser pattern design based on investigations of simplified TEG structures with the sintering profile $T_{max} = 1073$ K from Figure 5A. Ten samples with 12 measuring points each were examined

Parameter	Unsintered		Sintered		Scaling factor	
	Value [mm]	Rel. error (2σ) [%]	Value [mm]	Rel. error (2σ) [%]	Value [mm]	Rel. error (2σ) [%]
Cutting loss	0.24	22.6	-	-	-	-
Structuring width	0.31	14	0.15	28.6	0.49	42.6
Shrinkage	-	-	-	-	**0.89**	2
VIAS diameter	0.58	4.5	1.00	6	**1.72**	10.5

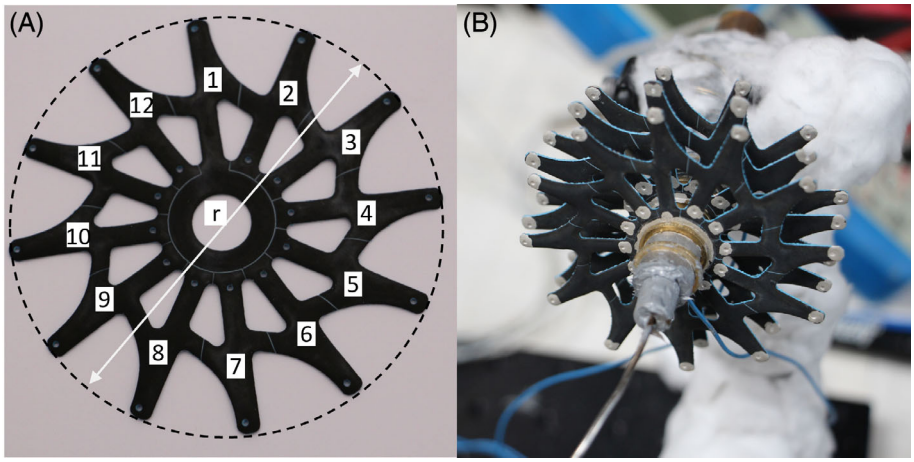

FIGURE 8 (A) Manufactured module after post-processing with reduced dimensions. To characterize the shrinkage, the lengths of the thermolegs (2–12) between the VIAS and the total radius of the module (r) were measured (see Table 3). (B) Fully assembled stack-TEG of 3 modules on a shaft

unsintered state, the size of the module is reduced by 10% after post-processing according to the measured values shown in Table 3.

The generated voltage and achievable power of a TEG increases with the temperature gradient across the thermocouple. The concept presented is based on modules that dissipate heat to the environment themselves due to their high surface area and do not use an additional heat sink. The geometry of the modules determines the size of this gradient. Numerous studies have already shown how the performance and efficiency of TEGs can be significantly increased by optimizing their geometry.[63–65] If the temperature distribution of the presented TEG can be modeled adequately, this will prospectively allow an individual optimization. Figure 9 shows a comparison of the expected temperature distribution of an FEM simulation (Figure 9A) and the real temperature distribution measured by IR-Cam (Figure 9B) for steady state conditions under free convection.

It is obvious that there is a clear shift in the temperature distribution along the vertical axis between model and measurement. While the thermocouples 12, 1 and 2 show higher temperatures in the center and larger gradients in total, the thermocouples 6–8 have an opposite distribution. Since the TEG module is symmetrical around the heat source, a similar temperature distribution for each of the 12 thermocouples would be expected. The reason for this shift is a nonuniform heat transfer caused by different thermal resistances between the shaft and the modules. Because of the required tolerances, there is a gap of several 100 µm between the module and the shaft, which is closed by a thermal gap filler (cf. Figure 3). As a result of the module's own weight, the thickness of this layer is not constant in all directions, it is smallest at the upper pairs 12, 1, and 2 and largest at the lower thermocouples 6–8. To confirm this, temperature distributions of one TEG in different rotation positions were measured and analyzed. The results are attached in the Supporting Information (Appendix S1). Table 4 summarizes the temperature distribution for each thermocouple and selected zones. Calculated from the mean value of all thermocouples, the gradients are 22% higher at the top and 25% lower at the bottom of the TEG module. On the other hand, if all remaining thermocouples that are located on or around the horizontal axis are combined

TABLE 3 Characteristic dimensions before and after post-processing and the resulting shrinkage of the TEG geometry for the module presented in Figure 8A

Thermocouple Nr.	Unsintered [mm]	Sintered [mm]	Scaling factor
2	25.42	23.00	0.9
3	25.37	22.84	0.9
4	25.56	22.99	0.9
5	25.48	22.78	0.89
6	25.36	23.04	0.91
7	25.39	22.92	0.9
8	25.54	22.76	0.89
9	25.39	22.63	0.89
10	25.50	22.79	0.89
11	25.53	22.84	0.89
12	25.54	22.80	0.89
r	81.4	72.55	0.89
2–12, *r*	-	-	$0.9 \pm 1.5\%$

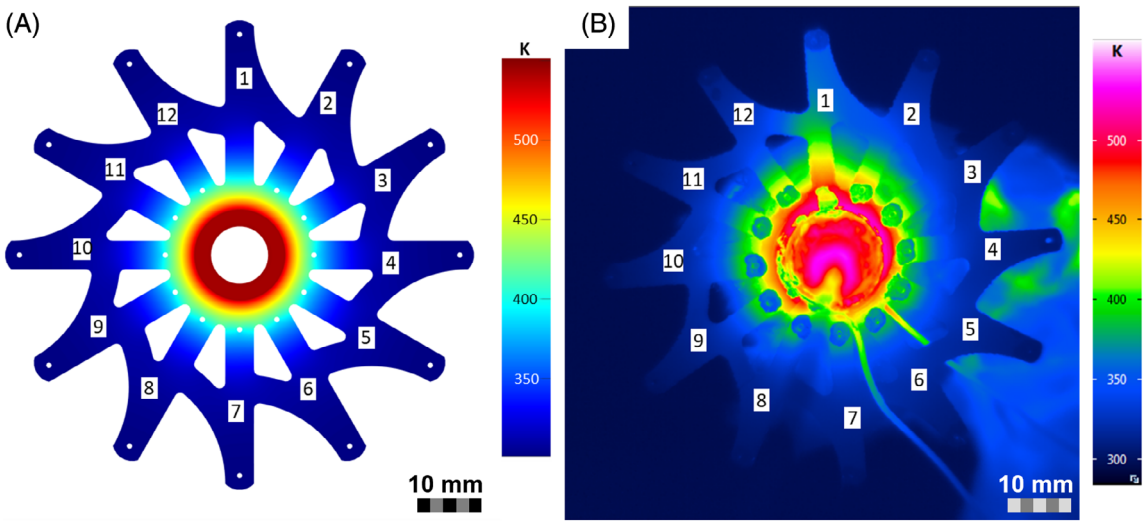

FIGURE 9 (A) FEM modeling of a temperature distribution inside a module in steady state with free convection. (B) Temperature distribution of a module in steady state after 45 min recorded by IR camera. The gradients for the thermocouples 1–12 are shown in Table 4 and were measured above and below the contact areas.

(3–5, 9–11), it can be seen that they have approximately the same mean value but only half as much variance. Across all thermocouples the hot side temperatures and the temperature gradients of the IR measurement are higher than the model. The average gradient of 86.9 K is about 6 K higher than the model predicted (80.4 K). In addition to the nonuniform heat transfer and convective effects, this could also be partially caused by a change in the thermal conductivity of the LTCC substrate. Because the sinter profile has a 50 K lower maximum temperature compared to the specification and the determined shrinkage is lower, the material value could be less than the manufacturer's specification. Despite the described differences, the temperature distribution can be adequately explained by the model. The averaged gradients deviate from the measured values by approx. 7%. By validating the thermal conductivity coefficients and considering the different

TABLE 4 Comparison of temperature gradients from FEM simulation and IR measurement. The gradients were measured for each thermocouple above and below the contact area. For combined measurements, the variances (s) are listed

	Thermocouple Nr.	T_{cold} (inside) [K]		T_{hot} (outside) [K]		ΔT [K]	
IR-measurement	1	308.7		426.8		118	
	2	302.1		401.3		99.3	
	3	306.6		398.7		92.1	
	4	303.2		382		78.8	
	5	305.6		373.5		67.9	
	6	302.1		366.8		64.7	
	7	302.2		368.3		66.1	
	8	302.6		382.7		80.1	
	9	302.5		387.2		84.6	
	10	303.5		395.7		92.2	
	11	308.7		409.2		100.6	
	12	364.1		462.8		98.6	
	1–12	309.3	s = 17.4	396.3	s = 27.3	86.9	s = 16.2
	1, 2, 12	327.2	s = 32	432.9	s = 27.3	105.8	s = 10.7
	3–5, 9–11	303.4	s = 1.6	391.30	s = 8.4	87.8	s = 8
	6–8	303.3	s = 0.3	369.5	s = 8.8	66.2	s = 8.5
FEM	1–12 (symmetrical)	301.2		381.6		80.4	

contact resistances between the shaft and the module, this value can be improved. These findings could be used to further increase the power electrical output or to use the material more efficiently. A rough calculation illustrates this. Based on the temperature distribution from the model in Figure 9, a temperature gradient of approx. 62 K is built up on average over the first 7 mm of the length of the thermoleg. If an average Seebeck coefficient of 80 $\mu V*K^{-1}$ is assumed for this range based on the measurement in Figure 7, about 5 mV voltage is generated per thermocouple. On the remaining approx. 13 mm of the thermoleg only 18 K difference is realized and with an estimated Seebeck coefficient of 75 $\mu V*K^{-1}$ about 1.35 mV thermoelectric voltage is generated. If the low temperature dependence of the electrical conductivity in this range is neglected (cf. Figure 7), this means that approx. 3.5 times the thermoelectric voltage is generated at only about one third of the length and the electrical line resistance. Due to the very low electrical conductivity of the CCO, its line resistance dominates the total internal resistance and thus the power output of the TEG. An effective approach to optimize the power outputs would therefore be to successively reduce the length of the legs. The advantage of the manufacturing process used here is that such adaptations can be directly implemented without changes to equipment, using only modified laser patterns. In addition, the length of each thermoleg could be individually adjusted to the asymmetric temperature distribution. Because the TEG also has the function of a heat sink, it is important to consider that every change in geometry interacts directly with the temperature distribution. The parameterization of the used model can be applied to estimate these effects in the future.

A single module, a 2-Stack-TEG and a 3-Stack-TEG were manufactured, assembled and measured in a final step. The power of the heating element was increased successively. The temperature gradients of the thermocouples were measured by a thermographic camera in steady state after 45 min. Figure 10A,B shows the voltage–current curves and resulting power curves for the single module TEG at increasing heating power. At a maximum hot-side temperature of 413 K and a temperature gradient of 106 K a maximum electrical power of 0.224 µW was generated over the 12 thermocouples. Figure 10C,D present a comparison of three TEGs, one with a single module, a second TEG with two modules (2-Stack) and a third TEG consisting of three modules (3-Stack). All TEGs are in a comparable state with regard to hot side temperature and temperature gradient. The single module reached a maximum power of 0.12 µW

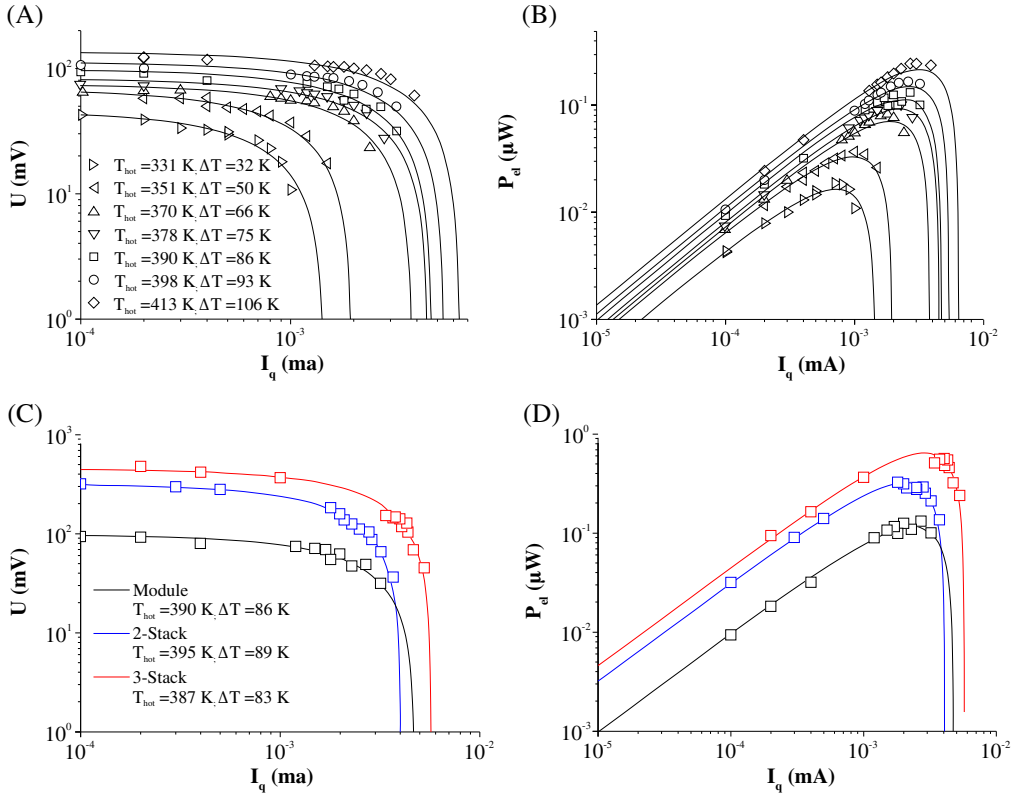

FIGURE 10 (A, B) Voltage-current curves and electrical power curves of a TEG from a single module for different hot side temperatures and temperature gradients. (C, D): Voltage–current curves and power curves of a single module TEG, a 2-Stack, and a 3-Stack TEG at comparable temperature gradients

(ΔT = 86 K, T_{hot} = 390 K), the 2-Stack 0.301 μW (ΔT = 85 K, T_{hot} = 395 K), and the 3-Stack 0.582 μW (ΔT = 83 K, T_{hot} = 387 K).

As a result, it was shown that the process presented is qualified to produce functional TEGs that are highly customizable to their application. Furthermore, the results demonstrate how TEGs manufactured in this way can be scaled through a modular approach. Together, the high level of customization, its simple realization and the modular design open the possibility to combine TEGs with locally different optimized geometries.

Table 5 summarizes the measurement results for the different TEGs. The characteristic values of the graphs from Figure 10A,B corresponding to the entries of the table with module quantity 1. The measurements of the three TEGs shown in Figure 10C,D are highlighted. A comparative analysis of the maximum power of the TEG stack of three modules with the generator presented by Jaziri et al. shows that the output achieved by the generator manufactured here is relatively low.[45] The Ag/PdAg TEG reached a performance more than two orders of magnitude higher than the CCO/Ag generator shown in this work, but at nearly three times the number of thermocouples and a 37% higher gradient. The second Ag/Ni-based TEG presented by Jaziri et al. also produced about eight times the power outputs, but with three times the number of thermocouples by 75% of the temperature gradient. Figure 7A,D show that the main reason for this is the low electrical conductivity of the CCO film. This could possibly be improved by mechanical compression of the film after spray-coating or an optimization of the sintering process. In general, the evaluation of other materials for the process presented here seems useful. With the goal of maximizing the power output, metallic material systems and half-Heusler alloys can be highly interesting options.[66] Pulsed nanosecond lasers or ultrashort pulse lasers would be attractive due to their finer structuring, lower heat input and more substrate-friendly processing and should be considered in the further development of the process.

TABLE 5 Characteristics of the TEGs for different temperature profiles and module quantities. Measured data for module quantity 1 correspond to the graphs in Figure 10A,B. The values used to compare the TEGs in Figure 10C,D are highlighted bold

Modules	$\overline{T_{hot}}$ [K]	$\overline{T_{cold}}$ [K]	$\overline{\Delta T}$ [K]	U_{OC} [mV]	I_{SC} [mA]	$P_{el,\,max}$ [µW]
1	330.8	298.9	32	45.879	0.0014	0.0169
	350.7	300.6	50.1	67.923	0.002	0.0359
	370.4	304.3	66.1	74.996	0.0038	0.0741
	378.2	302.9	75.4	81.951	0.0045	0.0965
	390.2	**304.3**	**85.9**	**98.145**	**0.0047**	**0.1201**
	398.2	304.8	93.5	112.23	0.0054	0.1561
	413.6	307	106.7	135.41	0.0064	0.224
2	325.3	296.6	28.7	68.777	0.0012	0.0209
	349	301	48	78.827	0.0026	0.0562
	379.9	302.6	77.3	253.54	0.0034	0.1947
	395.3	**306.7**	**88.6**	**319.28**	**0.0041**	**0.3068**
	409.1	308.7	100.6	344.36	0.0047	0.3864
3	321.8	295.9	25.9	130.53	0.0013	0.0414
	346.3	300.6	45.8	205.17	0.0023	0.125
	363.9	301.2	63	316.2	0.0032	0.2396
	368.1	300	68.2	349.52	0.0036	0.2635
	387.8	**304.4**	**83.4**	**454.88**	**0.0057**	**0.5819**

4 | CONCLUSION

A concept for the manufacturing of modular and stack-TEGs on LTCC substrates specifically designed for thermoelectric energy conversion of wasted heat on a shaft was presented. The process allows free design of the TEG geometry with high reproducibility of the dimensions after thermal post-processing. Suitable sintering profiles for combined post-processing of LTCC substrate and the thermoelectric films were identified. Symmetrical TEG modules were adapted to their application environment and combined to form a single generator. This is fully scalable by the number of modules. A stacked TEG of three modules with 12 thermocouples each reached a maximum electrical power of 0.5819 µW at $\overline{T_{\text{hot}}} = 387.8\text{K}$ and a temperature gradient of $\overline{\Delta T} = 83.4\text{K}$. A comparison of the temperature distribution from the FEM model and IR measurement shows that the heat transfer from the shaft to the TEG is not fully consistent due to manufacturing tolerances but can be described adequately well. Transferring the process approach to other material systems with higher electrical conductivities and laser sources with lower pulse widths has significant potential to greatly increase thermocouple density and improve generator performance.

The study shows that LTCC technology and laser structuring are well suited to producing temperature-resistant TEG with almost any geometry. As a maskless process, this offers the possibility of adapting TEG individually and specifically to different application environments and nonplanar connection surfaces with minimal effort. The modeling of the temperature distribution can be used in future to maximize the power output already during the design phase.

AUTHOR CONTRIBUTIONS

Marvin Abt: Conceptualization (lead); data curation (equal); investigation (lead); methodology (equal); visualization (lead); writing – original draft (lead). **Katharina Kruppa:** Conceptualization (equal); data curation (lead); visualization (equal); writing – review and editing (equal). **Mario Wolf:** Conceptualization (supporting); methodology (equal); visualization (equal); writing – original draft (equal); writing – review and editing (equal). **Armin Feldhoff:** Funding acquisition (lead); project administration (lead); writing – review and editing (lead). **Ludger Overmeyer:** Funding acquisition (lead); project administration (lead); writing – review and editing (lead).

ACKNOWLEDGMENT

This work was funded by the Deutsche Forschungsgemeinschaft (DFG, German Research Foundation) – project number 325156807. Open Access funding enabled and organized by Projekt DEAL.

CONFLICT OF INTEREST

The authors declare no conflict of interest.

PEER REVIEW

The peer review history for this article is available at https://publons.com/publon/10.1002/eng2.12590.

DATA AVAILABILITY STATEMENT

The data that support the findings of this study are available from the corresponding author upon reasonable request.

ORCID

Marvin Abt https://orcid.org/0000-0002-2138-3771
Katharina Kruppa https://orcid.org/0000-0002-3764-2109
Mario Wolf https://orcid.org/0000-0002-1567-5516
Armin Feldhoff https://orcid.org/0000-0003-1599-432X
Ludger Overmeyer https://orcid.org/0000-0002-7734-8895

REFERENCES

1. Rashid F, Joardder MUH. Future options of electricity generation for sustainable development: Trends and prospects. *Eng Rep*. 2020;4:e12508.
2. IEA, Global Energy Review. Assessing the Effects of Economic Recoveries on Global Energy Demand and CO2 Emissions in 2021; International Energy; 2021.
3. Zhang D, Wang Y, Yang Y. Design, performance, and application of thermoelectric nanogenerators. *Small*. 2019;15:e1805241. doi:10.1002/smll.201805241
4. Orr B, Akbarzadeh A, Mochizuki M, Singh R. A review of car waste heat recovery systems utilising thermoelectric generators and heat pipes. *Appl Therm Eng*. 2016;101:490-495.
5. Zhu B, Liu X, Wang Q, et al. Realizing record high performance in n-type Bi_2Te_3-based thermoelectric materials. *Energy Environ Sci*. 2020;13:2106-2114.
6. Zhang Q, Liao J, Tang Y, et al. Realizing a thermoelectric conversion efficiency of 12% in bismuth telluride/skutterudite segmented modules through full-parameter optimization and energy-loss minimized integration. *Energy Environ Sci*. 2017;10:956-963.
7. Liang Z, Xu C, Shang H, et al. High thermoelectric energy conversion efficiency of a unicouple of n-type Mg3Bi2 and p-type Bi2Te3. *Materi Today Phys*. 2021;19:100413.
8. NASA, Multi-Mission Radioisotope Thermoelectric Generator, National Aeronautics and Space Administration.
9. Franz BP, Glazoff MV. Investigation of oxygen sources and subsequent thorium oxidation in the iridium DOP-26 cladding material and PuO_2 fuel system. *Eng Rep*. 2020;2:e12285.
10. Araiz M, Casi Á, Catalán L, Martínez Á, Astrain D. Prospects of waste-heat recovery from a real industry using thermoelectric generators: Economic and power output analysis. *Energ Conver Manag*. 2020;2020:112376.
11. Ramírez R, Gutiérrez AS, Cabello Eras JJ, Valencia K, Hernández B, Duarte Forero J. Evaluation of the energy recovery potential of thermoelectric generators in diesel engines. *J Clean Prod*. 2019;241:118412.
12. Forman C, Muritala IK, Pardemann R, Meyer B. Estimating the global waste heat potential. *Renew Sustain Energy Rev*. 2016;57:1568-1579.
13. Al Musleh M, Topriska E, Jack L, Jenkins D. Thermoelectric generator experimental performance testing for wireless sensor network application in smart buildings. *MATEC Web Conf*. 2017;120:8003.
14. Narducci D. Thermoelectric harvesters and the internet of things: technological and economic drivers. *J Phys Energy*. 2019;1:24001.
15. Khan S, Kim J, Acharya S, Kim W. Review on the operation of wearable sensors through body heat harvesting based on thermoelectric devices. *Appl Phys Lett*. 2021;118:200501.
16. Attar A, Albatati F. Wearable thermoelectric generators as energy harvesters for wireless body sensors. *Int J Energy Environ Eng*. 2021;12:131-149.
17. Sujith A, Dorai DR, Kamalesh VN. Energy efficient zone-based clustering algorithm using fuzzy inference system for wireless sensor networks. *Eng Rep*. 2021;3:e12310.
18. Agrawal D, Pandey S. Load balanced fuzzy-based unequal clustering for wireless sensor networks assisted Internet of Things. *Eng Rep*. 2020;2:e12130.
19. Kishore RA, Priya S. A review on low-grade thermal energy harvesting: materials, methods and devices. *Materials*. 2018;11:1433.
20. Pourkiaei SM, Ahmadi MH, Sadeghzadeh M, et al. Thermoelectric cooler and thermoelectric generator devices: A review of present and potential applications, modeling and materials. *Energy*. 2019;186:115849.

21. LeBlanc S. Thermoelectric generators: Linking material properties and systems engineering for waste heat recovery applications. *Sustain Mater Technol*. 2014;1-2:26-35.
22. Wang Y, Yang L, Shi X-L, et al. Flexible thermoelectric materials and generators: challenges and innovations. *Adv Mater*. 2019;31:e1807916.
23. Du Y, Xu J, Paul B, Eklund P. Flexible thermoelectric materials and devices. *Appl Mater Today*. 2018;12:366-388.
24. Zhao X, Han W, Zhao C, et al. Fabrication of transparent paper-based flexible thermoelectric generator for wearable energy harvester using modified distributor printing technology. *ACS Appl Mater Interfaces*. 2019;11:10301-10309.
25. Stepien L, Roch A, Schlaier S, et al. Investigation of the thermoelectric power factor of KOH-treated pedot:pss dispersions for printing applications. *Energy Harvest Syst*. 2016;3:101-111.
26. Chen B, Kruse M, Xu B, et al. Flexible thermoelectric generators with inkjet-printed bismuth telluride nanowires and liquid metal contacts. *Nanoscale*. 2019;11:5222-5230.
27. Besganz A, Zöllmer V, Kun R, Pál E, Walder L, Busse M. Inkjet printing as a flexible technology for the deposition of thermoelectric composite structures. *Procedia Technol*. 2014;15:99-106.
28. Ou C, Sangle AL, Datta A, et al. Fully printed organic–inorganic nanocomposites for flexible thermoelectric applications. *ACS Appl Mater Interfaces*. 2018;2018:19580-19587.
29. Shin S, Kumar R, Roh JW, et al. High-Performance Screen-Printed Thermoelectric Films on Fabrics. *Sci Rep*. 2017;7:7317.
30. Rösch AG, Gall A, Aslan S, et al. Fully printed origami thermoelectric generators for energy-harvesting. *Npj Flex Electron*. 2021;5:1-8.
31. Comamala M, Pujol T, Cózar IR, Massaguer E, Massaguer A. Power and fuel economy of a radial automotive thermoelectric generator: experimental and numerical studies. *Energies*. 2018;11:2720.
32. Yuan Z, Tang X, Xu Z, et al. Screen-printed radial structure micro radioisotope thermoelectric generator. *Appl Energy*. 2018;225:746-754.
33. Weber J, Potje-Kamloth K, Haase F, Detemple P, Völklein F, Doll T. Coin-size coiled-up polymer foil thermoelectric power generator for wearable electronics. *Sens Actuat A Phys*. 2006;132:325-330.
34. Tappura K. A numerical study on the design trade-offs of a thin-film thermoelectric generator for large-area applications. *Renew Energy*. 2018;120:78-87.
35. He R, Schierning G, Nielsch K. Thermoelectric devices: a review of devices, architectures, and contact optimization. *Adv Mater Technol*. 2018;3:1700256.
36. Petsagkourakis I, Tybrandt K, Crispin X, Ohkubo I, Satoh N, Mori T. Thermoelectric materials and applications for energy harvesting power generation. *Sci Technol Adv Mater*. 2018;19:836-862.
37. Chen X, Dai W, Wu T, et al. Thin film thermoelectric materials: classification, characterization, and potential for wearable applications. *Coatings*. 2018;8:244.
38. Nozariasbmarz A, Collins H, Dsouza K, et al. Review of wearable thermoelectric energy harvesting: From body temperature to electronic systems. *Appl Energy*. 2020;258:114069.
39. Zeng M, Zavanelli D, Chen J, et al. Printing thermoelectric inks toward next-generation energy and thermal devices. *Chem Soc Rev*. 2022;51:485-512.
40. Zhu J, Yung WKC. Studies on laser ablation of low temperature co-fired ceramics (LTCC). *Int J Adv Manuf Technol*. 2009;42:696-702.
41. Gutzeit N, Schulz A, Fischer M, Thelemann T, Muller J. Picosecond laser structuring technology for LTCC - the improvement of fine line structuring. Proceedings of the 22nd European Microelectronics and Packaging Conference & Exhibition (EMPC); 2019:1-5.
42. Shafique MF, Saeed K, Steenson DP, Robertson ID. Laser prototyping of microwave circuits in LTCC technology. *IEEE Trans Microwave Theory Techn*. 2009;57:3254-3261.
43. Schulz A, Gutzeit N, Muller J. Laser structured passive components and RF filter in LTCC technology with operating frequencies up to 40 GHz focusing on 5G mobile applications. Proceedings of the 22nd European Microelectronics and Packaging Conference & Exhibition (EMPC); 2019:1-5.
44. Espera AH, Dizon JRC, Chen Q, Advincula RC. 3D-printing and advanced manufacturing for electronics. *Prog Addit Manuf*. 2019;4:245-267.
45. Jaziri N, Müller J, Müller B, et al. Low-temperature co-fired ceramic-based thermoelectric generator with cylindrical grooves for harvesting waste heat from power circuits. *Appl Therm Eng*. 2021;184:116367.
46. Markowski PM. Multilayer thick-film thermoelectric microgenerator based on LTCC technology. *Microelectron Int*. 2016;33:155-161.
47. Abt M, Wolf M, Feldhoff A, Overmeyer L. Combined spray-coating and laser structuring of thermoelectric ceramics. *J Mater Process Technol*. 2020;275:116319.
48. Wolf M, Abt M, Hoffmann G, Overmeyer L, Feldhoff A. Ceramic-based thermoelectric generator processed via spray-coating and laser structuring. *Open Ceramics*. 2020;1:100002.
49. Kwon K-S, Rahman MK, Phung TH, Hoath S, Jeong S, Kim JS. Review of digital printing technologies for electronic materials. *Flex Print Electron*. 2020;5:043003.
50. Villafuerte J. *Modern Cold Spray*. Springer International Publishing; 2015.
51. Bittner M, Geppert B, Kanas N, Singh SP, Wiik K, Feldhoff A. Oxide-based thermoelectric generator for high-temperature application using p-Type $Ca_3Co_4O_9$ and n-Type $In_{1.95}Sn_{0.05}O_3$ Legs. *Energy Harvest Syst*. 2016;3:213-222.
52. Wang C-C, Hung C-I, Chen W-H. Design of heat sink for improving the performance of thermoelectric generator using two-stage optimization. *Energy*. 2012;39:236-245.
53. LeBlanc S, Yee SK, Scullin ML, Dames C, Goodson KE. Material and manufacturing cost considerations for thermoelectrics. *Renew Sustain Energy Rev*. 2014;32:313-327.

54. Kordas K, Pap AE, Saavalainen J, et al. Laser-induced surface activation of LTCC materials for chemical metallization. *IEEE Trans Adv Packag*. 2005;28:259-263.
55. Kita J, Dziedzic A, Golonka LJ, Bochenek A. Properties of laser cut LTCC heaters. *Microelectron Reliab*. 2000;40:1005-1010.
56. Girardi MA, Peterson KA, Vianco PT, Grondin R, Wieliczka D. Laser ablation of thin films on LTCC. *Int Symp Microelectron*. 2014;2014:677-686.
57. Uno K. Longitudinally excited CO2 laser. In: Peshko I, ed. *Laser Pulses - Theory, Technology, and Applications*. InTech; 2012.
58. DuPont, DuPont™ GreenTape™ low temperature co-fired ceramic system. Design and Layout Guidelines; 2009. https://studylib.net/doc/18479645/dupont%E2%84%A2-greentape%E2%84%A2-design-and-layout-guidelines
59. Tahashi M, Tanimoto T, Goto H, Takahashi M, Ido T. Sintering temperature dependence of thermoelectric performance and crystal phase of calcium cobalt oxides. *J Am Ceram Soc*. 2010;93:3046-3048.
60. Lavrenko VA, Malyshevskaya AI, Kuznetsova LI, Litvinenko VF, Pavlikov VN. Features of high-temperature oxidation in air of silver and alloy Ag-Cu, and adsorption of oxygen on silver. *Powder Metall Met Ceram*. 2006;45:476-480.
61. Sursaeva VG, Straumal AB. Thermal stability of the microstructure of silver films. *Russ Metall*. 2017;2017:263-266.
62. Miyazaki Y, Onoda M, Oku T, et al. Modulated structure of the thermoelectric compound $[Ca_2CoO_3]_{0.62}CoO_2$. *J Phys Soc Japan*. 2002;71:491-497.
63. Karri NK, Mo C. Geometry optimization for structural reliability and performance of a thermoelectric generator. *SN Appl Sci*. 2019;1:1097.
64. He Z-Z. A coupled electrical-thermal impedance matching model for design optimization of thermoelectric generator. *Appl Energy*. 2020;269:115037.
65. Shittu S, Li G, Zhao X, Ma X. Review of thermoelectric geometry and structure optimization for performance enhancement. *Appl Energy*. 2020;268:115075.
66. Wolf M, Hinterding R, Feldhoff A. High power factor vs. high zT—a review of thermoelectric materials for high-temperature application. *Entropy*. 2019;21:1058.

AUTHOR BIOGRAPHIES

Marvin Abt studied chemical engineering at the Technical University of Dresden. Since 2017, he has been working at the Institut für Integrierte Produktion Hannover gGmbH as a project engineer and Ph.D. candidate in the field of thermoelectric and automation technology.

Katharina Kruppa studied Chemistry (B. Sc., M. Sc.) with major in General Chemistry at Leibniz University Hannover. Currently, she is working on her Ph.D. in the field of thermoelectric materials at the Leibniz Universität Hannover in the Institute for Physical Chemistry and Electrochemistry as part of a research cooperation between Lower Saxony and Israel, which is funded by the Lower Saxony Ministry of Science and Culture.

Mario Wolf studied (B.Sc.) and Materials Chemistry and Nanochemistry (M.Sc.) at Leibniz University Hannover. In 2021, he finished his Ph.D. in Chemistry at Leibniz University Hannover in the Institute of Physical Chemistry and Electrochemistry.

Armin Feldhoff holds a diploma in physics from the University of Münster and a Ph.D. degree from the Martin-Luther University Halle-Wittenberg. He was pre- and post-doctoral researcher at the Max Planck Institute of Microstructure Physics. He was postdoctoral associate at Cornell University in Ithaca (NY, USA) and at the French National Centre for Scientific Research (CNRS) in Vitry sur Seine. He obtained the venia legendi for Physical Chemistry in 2009, and since 2012 he has been extraordinary professor at the Faculty of Natural Sciences of Leibniz University Hannover.

Ludger Overmeyer studied Electrical Engineering at the Leibniz University Hannover and holds a Ph.D. degree in Mechanical Engineering. He worked as project manager, division manager and head of research and development at Mühlbauer AG in Roding. Since 2001 Ludger Overmeyer is Professor of Transport and Automation Technology of the Leibniz University Hannover.

SUPPORTING INFORMATION

Additional supporting information can be found online in the Supporting Information section at the end of this article.

How to cite this article: Abt M, Kruppa K, Wolf M, Feldhoff A, Overmeyer L. Experimental application of a laser-based manufacturing process to develop a free customizable, scalable thermoelectric generator demonstrated on a hot shaft. *Engineering Reports*. 2022;e12590. doi: 10.1002/eng2.12590